Rigid-Body Rotation Versus Transverse Bending Wave Swimming of Magnetically-Functionalized Sperm Cells

Veronika Magdanz[1], Anke Klingner[2], Leon Abelmann[3,4], and Islam S. M. Khalil[5]

***Abstract*— Cell membrane potential affects the electrostatic self-assembly of magnetizable nanoparticles around the flagellum of sperm cells, leading to the formation of biohybrid microrobots (i.e. IRONSperm) with various bending stiffness. Here we explain the influence of bull sperm cell membrane potential on the formation of two types of IRONSperm samples that are produced by electrostatic self-assembly. The first is a proximal-coated soft body with nanoparticles concentrated on the head to maintain high flexibility of the flagellum and create a passively propagating transverse bending wave under the influence of an external rotating magnetic field. The second is a rigid-body with nanoparticles approximately uniformly distributed along the length to provide arbitrary geometry that maintains a constant chiral shape and propel by rotation about its long axis. We present a magneto-elastohydrodynamic model to predict the swimming speed at low Reynolds number for rigid IRONSperm with arbitrary shapes, and show that decreasing the bending stiffness allows the model to capture the behavior of its soft counterpart. While the response of a rigid chiral IRONSperm is distinguished by a greater swimming speed with a smooth decay with frequency, the benefit of a soft flagellum in certain scenarios would present a much smaller range of frequencies for wireless actuation.**

I. INTRODUCTION

There is an increasing need for wireless autonomous microrobots that can perform important tasks such as sensing, diagnosis [1], [2], locomotion, actuation [3], and localized drug delivery [4]. A challenge with these active systems is the bulk fabrication of stimuli-responsive biocompatible materials at the micro scale; loading with concentrated doses of drugs and swimming efficiently at low Reynolds number (Re) hydrodynamics. One solution for the fabrication of such systems is a biohybrid approach, in which synthetic and biological components are self-assembled through electrostatic interactions into biohybrid microrobots with novel properties. In this framework, motile or immotile cells are integrated with inorganic components, that are developed by synthesis or microfabrication. Propulsive thrust can be directly produced by motile organisms [5] or by external magnetic fields [6]. In these biohybrid active systems, the inorganic component can provide additional functions (e.g., magnetic moment for wireless actuation [6], photothermal therapy [7], and contrast agents for noninvasive localization [8], [9]) that cannot be incorporated to the organisms through genetic engineering. The use of immotile organisms as elements for the propagation of mechanical waves makes the biohybrid microrobots less sensitive to chemical and biological conditions (e.g., pH, nutritional levels, temperature, lifetime of the cells) in the environment. Although maximum robustness to biological conditions can be obtained from the integration of immotile cells and inorganic components (Fig. 1(a)), the variation between the produced samples is significant, in terms of geometry, elasticity [10], and magnetization [11], for two key reasons. First, there is a variation of stiffness of the flagella influenced by the level of adenosine triphosphate (ATP), Mg, and other molecular levels inside the cell [17]. This leads to an intrinsic variation of bending stiffness. Sec-

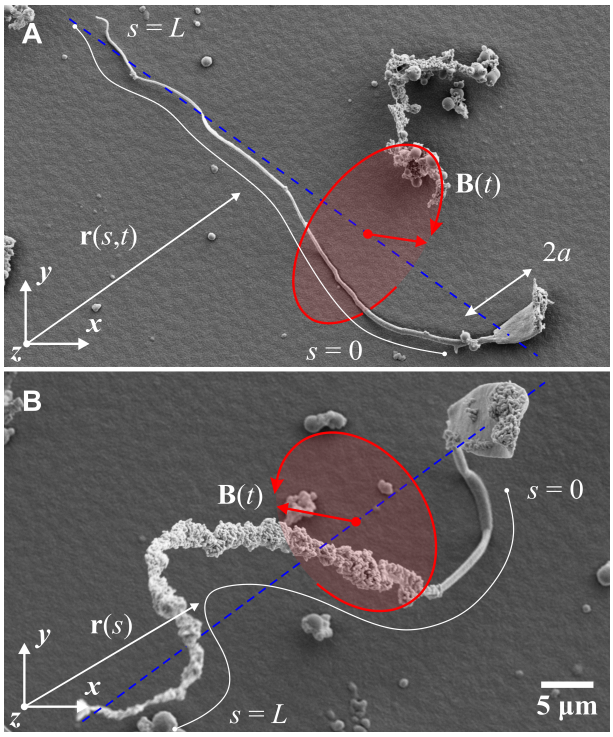

Fig. 1: The surface charge, $q_s(s)$, of the organic body varies along the arclength, $s \in [0, L]$, and across sperm cells, and yields intrinsic variable stiffness between samples. (A) Nanoparticle concentration small enough to provide a magnetic moment to bull sperm cells enables them to swim using propagating transverse waves in a rotating magnetic field. (B) Nanoparticle concentration large enough to provide rigid biohybrid structure allows for swimming by rigid-body rotation under the influence of a rotating magnetic field, $\mathbf{B}(t)$.

[1]V. Magdanz is with the Institute for Bioengineering of Catalonia, Barcelona Institute of Science and Technology, Barcelona, Spain (e-mail: vmagdanz@ibecbarcelona.eu).

[2]A. Klingner is with the Department of Physics, The German University in Cairo, New Cairo, Egypt.

[3]L. Abelmann is with MESA+ Research Institute, University of Twente, 7500 AE Enschede, The Netherlands.

[4]L. Abelmann is with KIST Europe, 66123 Saarbrucken, Germany.

[5]I. S. M. Khalil is with the Department of Biomechanical Engineering, University of Twente, 7500 AE Enschede, The Netherlands (e-mail: i.s.m.khalil@utwente.nl).

978-1-6654-5973-0/22/$31.00 ©2022 IEEE

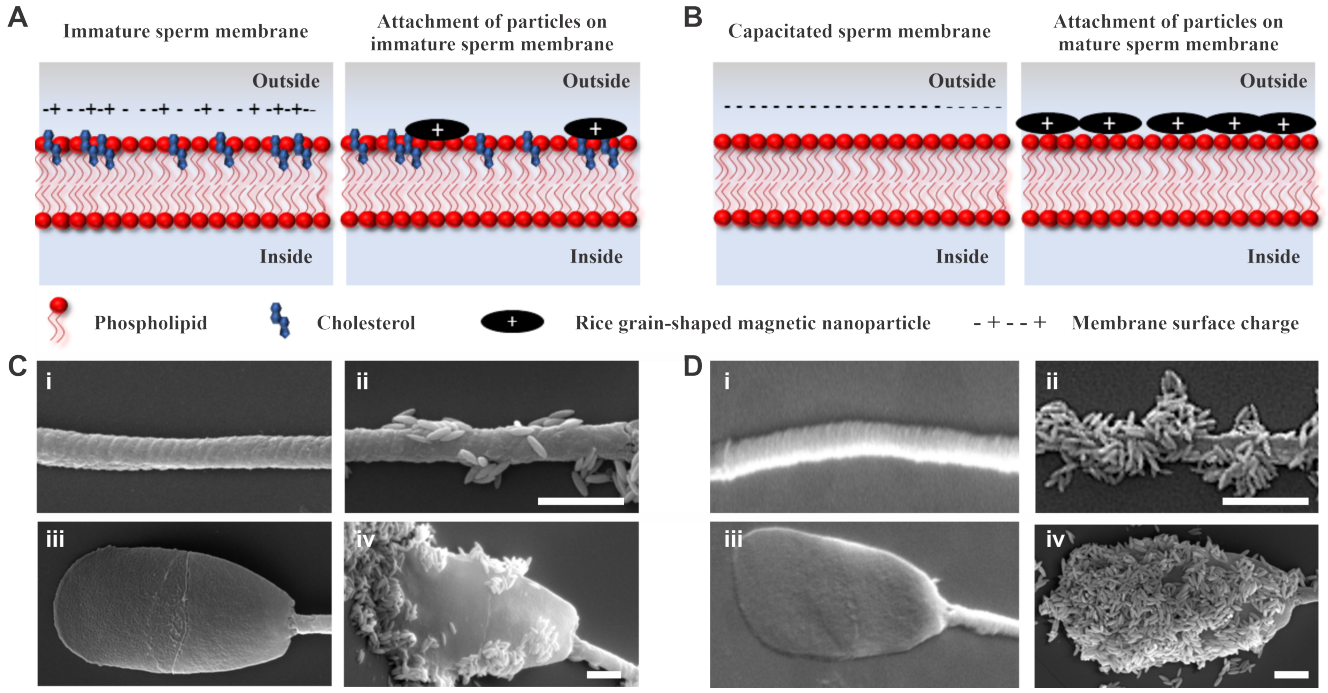

Fig. 2: The magnetic nanoparticle coating of IRONSperm is governed by the charge-distribution and composition of the membrane. (A) Cholesterol, among other components, is integrated in the membrane. (A-i) Immature cells consist of a negatively-charged lipid bilayer with a large portion of cholesterol which shifts the net membrane charge, q_s, to more neutral. (A-ii) Such cells, when exposed to positively charged nanoparticles create IRONSperm with few particles due to low electrostatic binding sites on their surface. (B-i) When sperm cells undergo the maturation process called capacitation, they shed cholesterol from the membrane which shifts the net charge of the membrane to a more negative value. (B-ii) This results in IRONSperm with high coverage of particles, due to strong electrostatic interactions. Scanning electron microscopic images of flagella membrane before particles attachment (C-i), (D-i), with few particles bound (C-ii) and high load of particles (D-ii). Electron microscopic images of sperm heads before particle attachment (C-iii), (D-iii), with few particles in case of low negative charge (C-iv) and highly negative charge (D-iv). A sperm sample usually has a population of immature and mature cells and the resulting IRONSperm population displays cells with full or partial coverage of nanoparticles. Scale bars are $1\,\mu\text{m}$.

ond, the membrane composition affects the surface charge, thereby changing the particle-membrane electrostatic interactions. Particularly, in spermatozoa, the membrane charge varies with the maturation state of the cell. This property leads to a variation of particle load on the flagella, also influencing the stiffness of the biohybrid microrobot. The cell membrane potential shows a significant difference between samples, leading to sporadically attached nanoparticles along the flagellum (Fig. 1(b)).

Microfabrication technologies allow us to add a specific structure, and thereby providing functions to a microorganism. Plant-based biotemplated magnetically propelled helical microswimmers have been fabricated using spiral water-conducting vessels of different plants and the sequential deposition of Ti and Ni layers enables rotation in human serum under the influence of a time-periodic magnetic field [12]. Similarly, Kamata *et al*. have presented a biotemplating process onto *Spirulina* surface to fabricate metal microcoils [13], using an electroless plating technique, which can generate smooth metal layers selectively. The results of this work suggest that mass production of helical geometries with magnetic functionality is possible. However, when selecting the material deposited on the *Spirulina* template, the selection of drug loading will be limited to surface functionalization and coating. Dip-coating is an alternative approach to add several functionalities to an organic body in a single-step fabrication process. Yan *et al*. have fabricated biohybrid magnetic microrobots by integrating *Spirulina* microalgae via a facile dip-coating process in a magnetite (i.e., Fe_3O_4) suspensions [8]. The resulting microrobot exhibits intrinsic fluorescence, natural degradability, and desirable cytotoxicity. These microrobots can swim or roll on a nearby solid boundary by rigid-body rotation using an external magnetic field [6]. Similarly, it has been shown that sperm cells can be coated by magnetizable nanoparticles and achieve drag-based propulsion in low-Re using rotating magnetic fields. Such microrobots are promising candidates for drug delivery and *in vivo* imaging of spermatozoa. This self-assembly based fabrication of magnetic sperm-templated microrobots results in a variety of swimmers, which were characterized and categorized in a previous study [11]. In this article, the focus is on the underlying reasons for the differences in particle coating and the resulting flexibility of the magnetic swimmers. The membrane charge of the cells significantly affect the nanoparticle coating, resulting in *at least* two swimming modes using drag-based propulsion: swimming by rigid-body rotation and swimming by transverse bending wave propagating along a flexible tail, both under the influence of a rotating magnetic field.

In this paper, we focus on the important effect of the

surface charge of the cell membrane on the mechanical and magnetic properties of nanoparticle-coated sperm cells (i.e., IRONSperm). Further, we model the influence of these properties on the deformation of IRONSperm. A three-dimensional (3-D) magneto-elastohydrodynamic model enables us to determine the swimming speed and propulsive thrust of rigid bodies with arbitrary initial deformations and show that decreasing the bending stiffness allows the model to capture the behavior of the soft IRONSperm.

II. INFLUENCE OF CELL MEMBRANE POTENTIAL ON THE PROPULSION MECHANISM

The self-assembly of spermatozoa with surface charge $q_{\mathrm{s}}(s)$ and rice grain-shaped magnetic particles with charge q_{p} relies on the electrostatic interaction between the negatively-charged areas of the cell membrane and positively charged nanoparticles, $q_{\mathrm{p}}q_{\mathrm{s}}(s)/(4\pi\epsilon_0 z^2)$, where ϵ_0 and z are the permittivity and closest separation distance between particles and a point along the arclength s, respectively. This interaction has led to a variety of sperm-particle constructs in terms of surface coverage and location of the magnetizable nanoparticles, leading to a wide variety of responses to the rotating magnetic field [11], [15]. The elongated shape of the nanoparticles contributes to an enhanced overall magnetization due to their alignment. Note that spherical particles have been tested previously and did not result in a comparable magnetic moment to that of the rice-shaped particles.

A. Membrane Charge of IRONSperm

One reason for the different coverage of rice grain-shaped magnetic particles on the sperm membranes can be seen in the variation of charges across the membrane. This property is governed by the compositions of the double lipid membrane with glycoproteins and other intercalated macromolecules in the membrane (Fig. 2). This composition changes during the lifetime of the spermatozoa. In particular, cholesterol ($C_{27}H_{46}O$) is abundantly embedded in the membrane and released upon maturation. The presence of cholesterol affects the membrane fluidity, facilitates cell signaling and helps maintain the integrity of these membranes. Cholesterol can make up nearly half of the membrane by molecular number. It is smaller and weighs less than other molecules in the cell membrane, so that it makes up a lesser proportion of the cell membrane's mass, approximately 20%. Cholesterol adds firmness and integrity to the plasma membrane. The presence of cholesterol reduces indirectly the negative surface charge of membranes, by allowing sodium ion (Na+) binding and thus turning it more neutral [16].

B. Charge-Distribution and Bending Stiffness

The heterogeneous membrane structure is important to regulate different cell functions such as protein uptake or signalling. The changes in membrane composition are driven by maturation processes which prepare the cell for the final step of fusion with the oocyte at the time of fertilization. Overall, the net charge of most cells is negative, $\langle q_{\mathrm{s}}(s)\rangle < 0$, however this can vary from cell to cell. Besides the composition of the lipid raft of the membrane, external conditions also play a role such as pH, temperature, and ionic concentrations [14]. The influence of the environmental factors are avoided by washing the cells in de-ionized water before incubating them with the positively charged magnetic nanoparticles. Thus, when exposed to positively charged nanoparticles, the amount of particles that electrostatically bound to the surface correlates with the initial net negative charge of the cell at the point of charge equilibrium. This results in a relatively higher or lower concentration on the surface. A high particle concentration results in rigid IRONSperm (Figs. 2B and 2D), while a low concentration, scattered particle binding leads to flexible IRONSperm (Figs. 2A and 2C).

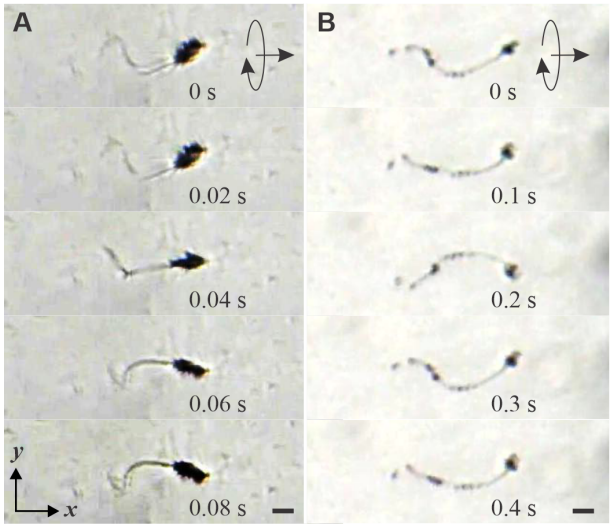

Fig. 3: Soft (A) and rigid (B) IRONSperm samples swim by drag-based propulsion using an external rotating magnetic field with a field rotation-axis along the direction of motion. (A) A proximal-coated IRONSperm swims by passively propagating waves initiated from the rotation of the head. (B) The bending stiffness of a fully-coated IRONSperm is much greater than any other partially-coated cell and it is likely to undergo rigid-body rotations about its long axis. Scale bars are $10\,\mu\mathrm{m}$.

III. DRAG-BASED THRUST OF FLAGELLUM WITH INTRINSIC VARIABLE STIFFNESS

When an IRONSperm of bending stiffness κ and total length L is submerged in a viscous fluid and is subject to an external rotating magnetic field $\mathbf{B}(t)$, it will move using drag-based propulsion attributed to propagating transverse waves (Fig. 3(a)) along the length or rigid-body rotation with angular frequency $\omega = 2\pi f$ (Fig. 3(b)), where f is the frequency of rotation.

A. Hydrodynamic Drag Force and Torque

The bending stiffness of the flagellum dictates the swimming mode of IRONSperm. In the case of a flexible flagellum that undergoes elastic bending deformations, the propulsion is established by the wave propagation. The time taken by a propagating wave to spread along the flagellum scales as $\xi_\perp L^4/\kappa$, where $\xi_\perp = 4\pi\eta/\ln(L/r_{\mathrm{f}})$ is the perpendicular drag coefficient of a flagellum with a radius r_{f}. In a proximal-

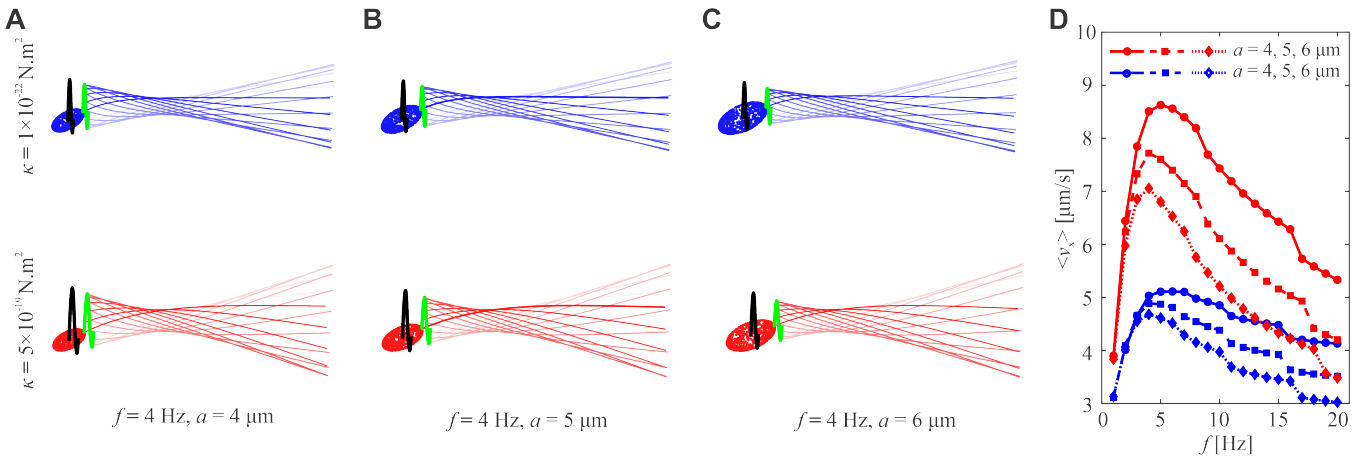

Fig. 4: Wave-pattern and swimming speed are calculated for actuation frequency $f \in [1, 20]$ Hz, sperm head length $2a = 8,\ 10,\ 12\,\mu$m, and bending stiffness $\kappa = 1 \times 10^{-22}$ and $\kappa = 5 \times 10^{-19}$ N.m^2. The curves represent the flagellum at equal time intervals over one beat cycle and the darker curves indicate later times. (A)-(C) The wave-pattern does not depend on the size of the head and the flagellum exhibits greater bending amplitude for higher bending stiffness. The black and green curves represent the position of the head and the proximal end of the flagellum over one period. (D) The time-averaged swimming speed, $\langle v_x \rangle$, increases with the bending stiffness and decreases with the size of the sperm head. Proximal coating is likely to increase the length of the head, leading to drag but no thrust.

or distal-coated flagellum, the bending stiffness is likely to be dependent on the condition of the membrane resulting in lower values of κ. When the magnetizable nanoparticles are distributed along the length, their concentration affect the bending stiffness. For both cases, in low-Re we have

$$\frac{\xi_\perp}{\kappa}\frac{\partial \mathbf{r}}{\partial t} = \frac{\partial^4}{\partial s^4}\left(\mathbf{r} - \mathbf{r}_0\right), \tag{1}$$

where $\mathbf{r}(s,t)$ is the position vector of points along the centerline of the flagellum with respect to a frame of reference (Fig. 1). The centerline is parameterized by the arclength s, $0 \le s \le L$. When the flagellum is bent into a curved chiral shape, the initial configuration is characterized by $\mathbf{r}_0 = \mathbf{r}(s,0)$. Note that the elastohydrodynamics of the flagellum is nondimensionalized by κ/L^2, and the dimensionless sperm-compliance number $\mathcal{L}$ is given by [18]

$$\mathcal{L} = L\left(\frac{\xi_\perp \omega}{\kappa}\right)^{1/4}. \tag{2}$$

The contribution of the bending stiffness, κ, to the sperm-compliance number allows the elastohydrodynamics described by Equation (1) to capture the two swimming modes. If the flagellum is rigid, $\mathcal{L} \ll 1$, then the left-hand side in Equation (1) vanishes, $\mathcal{L}\partial\mathbf{r}/\partial t \approx 0$. By integrating the right-hand side of Equation (1) over s, we can expect $\mathbf{r}(s,t)$ to be identically equal to $\mathbf{r}_0(s,0)$ on the interval $s \in [0, L]$. Now consider the same flagellum, but with lower value of κ, resulting in greater values of $\mathcal{L}$ for the same geometric, L, rheological, $\xi_\perp$, and actuation, ω, parameters. In this case, a magnetically-induced bending in shape spreads along the length at a rate proportional to $1/\kappa$. Therefore, we can use Equation (1) to capture two swimming modes of rigid and flexible IRONSperm by calculating $\mathbf{r}(s,t)$ for a range of κ.

Consider a rigid flagellum bent into a chiral shape and a flexible flagellum characterized by $\mathbf{r}(s,0)$ and $\mathbf{r}(s,t)$, respectively. The local velocity components along the flagellum are $\mathbf{v}_\parallel = [\dot{\mathbf{r}} \cdot \mathbf{t}]\mathbf{t}$ and $\mathbf{v}_\perp = \dot{\mathbf{r}} - \mathbf{v}_\parallel$ along the local tangent, $\mathbf{t}$, and normal directions to the centerline, respectively [19]. The relation between the hydrodynamic drag force, $\mathbf{f}(s,t)$ or $\mathbf{f}(s)$, and the velocity components is linear, we obtain

$$\mathbf{f}(s,t) = \xi_\perp \mathbf{v}_\perp(s,t) + \xi_\parallel \mathbf{v}_\parallel(s,t), \tag{3}$$

where $\xi_\parallel$ is the parallel fluid dynamic resistance coefficient. Since IRONSperm is freely swimming, the total hydrodynamic drag force and moment balance are given by

$$\mathbf{F}_\mathrm{h}(t) + \int_0^L \mathrm{d}s\mathbf{f}(s,t) = 0. \tag{4}$$

Here $\mathbf{F}_\mathrm{h} = 6\pi a \mathbf{C}\mathbf{v}_\mathrm{h}$ is the viscous drag force of the head of length $2a$ and velocity $\mathbf{v}_\mathrm{h}$ (Fig. 1(A)), where $\mathbf{C}$ is a matrix of resistive coefficients. Note that unlike the flagellum, the head contributes drag but not thrust and the swimming speed can be determined using the force balance (4) regardless of the chiral shape of the rigid flagellum or the stiffness of the flexible flagellum. The proximal coating is likely to play a role in the viscous drag by increasing the size (i.e., $2a$). The hydrodynamic drag moment balance is given by

$$\mathbf{M}_\mathrm{m}(t) + \mathbf{M}_\mathrm{h}(t) + \int_0^L \mathrm{d}s\mathbf{f}(s,t) \times \mathbf{r}(s,t) = 0, \tag{5}$$

where $\mathbf{M}_\mathrm{h}$ is the drag moment on the head and $\mathbf{M}_\mathrm{m}$ is the external magnetic torque. Equations (4) and (5) complete the hydrodynamics of IRONSperm and the instantaneous linear and angular velocities can be determined for a given bending stiffness, κ, and the contribution of the magnetic torque can be entered into the moment balance (5) using $\mathbf{M}_\mathrm{m}(t) = \mathbf{m}_\mathrm{h} \times \mathbf{B}(t)$. The imposed magnetic moment from a rotating magnetic field about the field-rotation axis, $\widehat{\boldsymbol{\omega}}_\mathrm{m}$, allows a rigid IRONSperm to undergo rigid-body rotation,

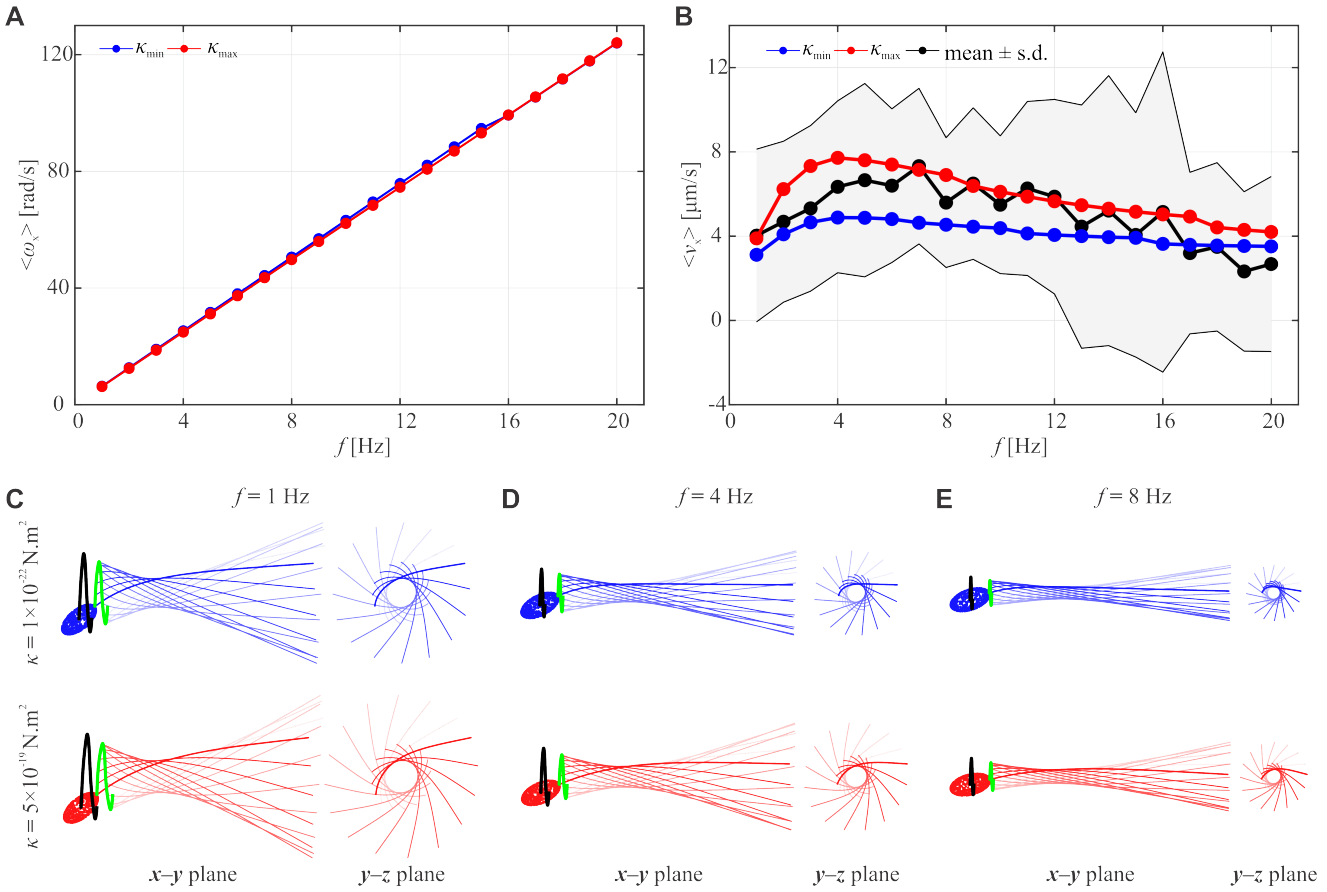

Fig. 5: Frequency response of a flexible (blue), $\kappa_{\min}$, and rigid (red), $\kappa_{\max}$, IRONSperm is calculated using equations (4) and (5). The time-averaged angular $\langle\omega_x\rangle$ and translational speeds $\langle v_x\rangle$, along the $\boldsymbol{x}$-axis are calculated over one period of rotation at each actuation frequency, f. (A) Rotational speed of flexible and rigid IRONSperm over rotating frequency. (B) Translational speed over frequency for flexible (blue), rigid (red) and mean (experimental results of IRONSperm with a range of nanoparticle coating). The step-out frequency of a rigid IRONSperm is greater than that of a flexible IRONSperm. For a rigid IRONSperm, $\langle v_x\rangle$ increases and falls off gradually with the frequency. The soft IRONSperm has a greater step-out frequency and its speed decreases gradually with f. (C) IRONSperm with flagellum of bending stiffness $\kappa = 1\times10^{-22}$ N.m^2 (blue, top) and $\kappa = 5\times10^{-19}$ N.m^2 (red, top) exhibits approximately similar wave-patterns with a decreasing envelop of motion for the increasing f. Increasing κ of the flagellum allows greater bending amplitude regardless of f. The black and green curves represent the position of the head and the proximal end of the flagellum over one period.

while a soft IRONSperm would deform differently at different frequencies allowing 3-D helical waves to propagate.

B. Numerical Simulation of the Swimming Path

Numerical calculations of the swimming behavior are implemented for one configuration of magnetic torque with field-rotation axis $\widehat{\boldsymbol{\omega}}_{\mathrm{m}} = [-1, 0, 0]^T$ in the coordinate system depicted in Fig. 1. The magnetic torque is produced using a rotating magnetic field at 45° with $\widehat{\boldsymbol{\omega}}_{\mathrm{m}}$. The geometrical and rheological characteristics of the numerical scheme are fixed such that the influence of the swimming behavior is influenced only by the bending stiffness in the $\kappa_{\min} \leq \kappa \leq \kappa_{\max}$ range, where $\kappa_{\min}$ represents the lowest bending stiffness of the flagellum and $\kappa_{\max}$ represents the greatest bending stiffness. Note that the proximal coating is likely to yield lowest bending stiffness as the flagellum is fully free of nanoparticles. In this case the energy is fed in by the magnetic torque acting only on the head and its magnitude is limited by the area of the negatively-charged regions. The amount of particles, and therefore the magnetic moment increases with the charged surface area. The surface area of the head is proportional to square of head radius, whereas the surface area of the flagellum is proportional to tail length, L, and tail diameter. Overall, the surface area of a sperm head is approximately twice as large as surface area of flagellum. Therefore, the magnetic moment of the head is greater than that of the flagellum. For both cases (i.e., rigid and soft), the magnitude of the moment is roughly constant.

Finite difference method is used to solve Equation (1) for each frequency using $\partial\mathbf{r}/\partial t = \widehat{\boldsymbol{\omega}}_{\mathrm{m}} \times \mathbf{r}$ and boundary conditions for free distal end, i.e., $\partial^2\mathbf{r}/\partial s^2|_{s=L} = 0$ and $\partial^3\mathbf{r}/\partial s^3|_{s=L} = 0$, and alignment of sperm cell head with magnetic field inclination relative to rotation axis of 45° ($\widehat{\boldsymbol{\omega}}^T\mathbf{r}|_{s=0} = |\mathbf{r}(s=0)|\cos 45°$). The initial shape is a straight filament (i.e., $\mathbf{r}_0 = 0$). With the field-rotation axis aligned along the $\boldsymbol{x}$-axis and the field being allowed to rotate at $f \in [1, 20]$ Hz, the position of the head is calculated during drag-based propulsion for the soft and rigid flagellum (Fig. 4). In the case of a soft and a rigid flagellum with

bending stiffness of $\kappa = 1 \times 10^{-22}$ and $\kappa = 5 \times 10^{-19}$ N.m^2, respectively, the head follows a rotating spiral vortex in the $\boldsymbol{y}$-$\boldsymbol{z}$ plane. The wave-pattern does not depend on the length (size) of the head ($2a$) for a given actuation frequency, as shown in Figs. 4(A) and 4(B). However, bending amplitude of the wave-pattern exhibits an increase with the bending stiffness, leading to significantly different frequency response and swimming speeds (Fig. 4(D)).

The instantaneous angular velocities of the soft and rigid IRONsperm indicate that their behavior to a rotating magnetic field is similar (Fig. 5(A)). Note that unlike the angular velocity case, the translational velocity of the rigid IRONSperm is greater than that of the soft IRONSperm, as shown in Fig. 5(B). For both cases, the time-averaged translational velocity, $\langle v_x \rangle$, increases below the step-out frequency and decreases approximately linearly on f. Measurements of the swimming speed of distal-coated and fully coated IRONSperm samples are shown in Fig. 5(B) using the black curve ($n = 22$). We do not observe close quantitative agreement between the measured frequency response and the numerical results. However, the measured frequency response is bounded by the predicted frequency response of the rigid and flexible IRONSperm.

There is a noticeable difference between the drag-based propulsion using rigid-body rotation and transverse bending waves throughout the frequency range; although the geometrical, rheological, and magnetic characteristics are related. The physical reasons are the following: (a) when the flagellum is fully coated with nanoparticles and its chiral shape is less dependent on frequency (Figs. 5(C)-5(E)), portions of the flagellum will contribute drag and others will contribute thrust. Consider, for example, the $1 \leq f \leq 8$ Hz range for the rigid IRONSperm, the translational speed depends nonlinearly on f, although the rotational velocity increases linearly with f. (b) a proximal-coated flagellum deforms and its shape depends on the frequency (Fig. 5(C)-5(E)). In this case, all portions of the flagellum contribute to generating propulsion while the magnetizable head contributes drag.

IV. CONCLUSIONS

When magnetizable nanoparticles are electrostatically assembled around the organic body of sperm cells, the resulting biohybrid microrobots (i.e., IRONSperm) will likely possess high flexibility or rigidity based on their original biochemical composition in terms of the cholesterol levels and other biomolecular contents of the membrane. The cholesterol level directly affects the membrane fluidity, integrity, and surface charge, and thereby affecting the bending stiffness of IRONSperm. We show that in the limits of small and large bending stiffness (originating from the membrane composition and/or the nanoparticle coating) two drag-based propulsion modes can be observed. In the first mode, swimming is achieved by rigid-body rotation and the frequency response depends on the original chiral shape that is formed after self-assembly. The second mode depends on propagating bending waves from the proximal end toward the distal end. In future studies, the maturation state of the spermatozoa will be controlled by inducing capacitation by incubation with maturation chemicals, e.g., heparin, bovine serum or progesterone, and thereby obtain a certain cohort of sperm cells with specific membrane charge. This article emphasizes the importance of physical and biochemical peculiarities of biohybrid microrobots that should be taken into account for precision control and actuation.

REFERENCES

[1] B. J. Nelson, I. K. Kaliakatsos, J. J. Abbott, "Microrobots for minimally invasive medicine," *Annu. Rev. Biomed. Eng.*, vol. 12, pp. 55–85, 2010.

[2] M. Sitti, H. Ceylan, W. Hu, J. Giltinan, M. Turan, S. Yim, E. Diller, "Biomedical applications of untethered mobile milli/microrobots," *Proc. IEEE Inst. Electr. Electron. Eng.*, vol. 103, pp. 205–224, 2015.

[3] L. Zhang, T. Petit, Y. Lu, B. E. Kratochvil, K. E. Peyer, R. Pei, J. Lou, B. J. Nelson, "Controlled propulsion and cargo transport of rotating nickel nanowires near a patterned solid surface," *ACS Nano*, vol. 4, pp. 6228–6234, 2010.

[4] M. P. Kummer, J. J. Abbott, B. E. Kratochvil, R. Borer, A. Sengul, and B. J. Nelson, "OctoMag: An electromagnetic system for 5-DOF wireless micromanipulation," *IEEE Trans. Robot.*, vol. 26, pp. 1006–1017, 2010.

[5] B. Behkam and M. Sitti, "Bacterial flagella-based propulsion and on/off motion control of microscale objects," *Appl. Phys. Lett.*, vol. 90, 023902, 2007.

[6] V. Magdanz, J. Gebauer, D. Mahdi, J. Simmchen, and I. S. M. Khalil, in *International Conference on Manipulation, Automation and Robotics at Small Scales (MARSS),* 2019, pp. 1–6.

[7] X. Huang, P. K. Jain, Ivan H El-Sayed, and M. A El-Sayed, "Plasmonic photothermal therapy (PPTT) using gold nanoparticles," *Lasers in Medical Science*, vol. 23, pp. 217–28, 2008.

[8] X. Yan, Q. Zhou, M. Vincent, Y. Deng, J. Yu, J. Xu, T. Xu, T. Tang, L. Bian, Y.-X. J. Wang, K. Kostarelos, and L. Zhang, "Multifunctional biohybrid magnetite microrobots for imaging-guided therapy," *Sci. Robot.*, vol. 2, eaaq1155, 2017.

[9] H. B. Na, I. C. Song, and T. Hyeon, "Inorganic Nanoparticles for MRI contrast agents," *Adv. Mat.*, vol. 21, pp. 2133-2148, 2009.

[10] J. M. S. Dias, D. Estima, H. Punte, A. Klingner, L. Marques, V. Magdanz, and I. S. M. Khalil, "Modeling and characterization of the passive bending stiffness of nanoparticle-coated sperm cells using magnetic excitation," *Adv. The. Sim.*, vol. 5, 2100438, 2022.

[11] V. Magdanz, J. Vivaldi, S. Mohanty, A. Klingner, M. Vendittelli, J. Simmchen, S. Misra, and I. S. M. Khalil, "Impact of segmented magnetization on the flagellar propulsion of sperm-templated microrobots," *Adv. Sci.*, vol. 8, 2004037, 2021.

[12] W. Gao, X. Feng, A. Pei, C. R. Kane, R. Tam, C. Hennessy, and J. Wang, "Bioinspired helical microswimmers based on vascular plants," *Nano Lett.*, vol. 14, pp. 305–310, 2014.

[13] K. Kamata, Z. Piao, S. Suzuki, T. Fujimori, W. Tajiri, K. Nagai, T. Iyoda, A. Yamada, T. Hayakawa, M. Ishiwara, S. Horaguchi, A. Belay, T. Tanaka, K. Takano, and M. Hangyo, "Spirulina-templated metal microcoils with controlled helical structures for THz electromagnetic responses," *Sci. Rep.*, vol. 4, 4919, 2015.

[14] L. H. Klausen, T. Fuhs, and M. Dong, "Mapping surface charge density of lipid bilayers by quantitative surface conductivity microscopy," *Nature communications*, vol. 7, 12447, 2016.

[15] V. Magdanz, J. Gebauer, P. Sharan, S. Eltoukhy, D. Voigt, and J. Simmchen, "Sperm–Particle interactions and their prospects for charge mapping," *Adv. Biosys.*, vol. 3, 1900061, 2019.

[16] A. Magarkar, V. Dhawan, P. Kallinteri, T. Viitala, M. Elmowafy, T. Róg, and A. Bunker, "Cholesterol level affects surface charge of lipid membranes in saline solution," *Sci. Rep.* vol. 4, 5005, 2014.

[17] K.A. Lesich, T. G. de Pinho, L. Dang, and C. B. Lindemann, "Ultrastructural evidence that motility changes caused by variations in ATP, Mg2+, and ADP correlate to conformational changes in reactivated bull sperm axonemes," *Cytoskeleton*, vol. 71, pp. 649-661, 2014.

[18] H. Gadelha, "On the Optimal Shape of Magnetic Swimmers," *Regular and Chaotic Dynamics*, vol. 18, pp. 75-84, 2013.

[19] B. M. Friedrich, I. H. Riedel-Kruse, J. Howard, and F. Jülicher, "High-precision tracking of sperm swimming fine structure provides strong test of resistive force theory," *The Journal of Experimental Biology*, vol. 213, pp. 1226-1234, 2010.